nature materials

Letter

https://doi.org/10.1038/s41563-023-01478-4

Proximity-induced superconductivity in epitaxial topological insulator/graphene/gallium heterostructures

In the format provided by the authors and unedited

Supplementary Information:

Proximity-Induced Superconductivity in Epitaxial Topological Insulator/Graphene/Gallium Heterostructures

Cequn Li[1], Yi-Fan Zhao[1], Alexander Vera[2,3], Omri Lesser[4], Hemian Yi[1], Shalini Kumari[2,3], Zijie Yan[1], Chengye Dong[5], Timothy Bowen[2,3], Ke Wang[6], Haiying Wang[6], Jessica L. Thompson[7], Kenji Watanabe[8], Takashi Taniguchi[9], Danielle Reifsnyder Hickey[3,6,7], Yuval Oreg[4], Joshua A. Robinson[1,2,3,5,6,7], Cui-Zu Chang[1], and Jun Zhu[1,2,5*]

1. Department of Physics, The Pennsylvania State University, University Park, PA 16802, USA
2. Center for 2-Dimensional and Layered Materials, The Pennsylvania State University, University Park, PA 16802, USA
3. Department of Materials Science and Engineering, The Pennsylvania State University, University Park, PA 16802, USA
4. Department of Condensed Matter Physics, Weizmann Institute of Science, Rehovot 760001, Israel
5. 2-Dimensional Crystal Consortium, The Pennsylvania State University, University Park, PA 16802, USA.
6. Materials Research Institute, The Pennsylvania State University, University Park, PA 16802, USA
7. Department of Chemistry, The Pennsylvania State University, University Park, PA 16802, USA
8. Research Center for Functional Materials, National Institute for Materials Science, 1-1 Namiki, Tsukuba 305-0044, Japan
9. International Center for Materials Nanoarchitectonics, National Institute for Materials Science, 1-1 Namiki, Tsukuba 305-0044, Japan.

* Correspondence to: jzhu@phys.psu.edu (J. Zhu)

Contents

1. Additional ARPES measurements 2
2. Fabrication of van der Waals tunnel junction 3
3. Four-terminal transport on BST/Gr/Ga 4
4. Fitting the tunneling spectra on Gr/Ga using the Blonder-Tinkham-Klapwijk model 6
5. Two-gap BTK fits on the 5QL and 10QL BST/Gr/Ga heterostructures 7
6. Evidence of Abrikosov vortex probed by tunneling conductance 11

1. Additional ARPES measurements

Figure S1 shows the ARPES band maps of 5-10QL $(Bi_{0.7}Sb_{0.3})_2Te_3$/Gr/Ga (BST/Gr/Ga) heterostructures. In each panel, the Fermi level resides in the Dirac surface states of the $(Bi_{0.7}Sb_{0.3})_2Te_3$ film. The Dirac point shifts from -200 meV to -170 meV as the film thickness increases from 5QL to 10QL.

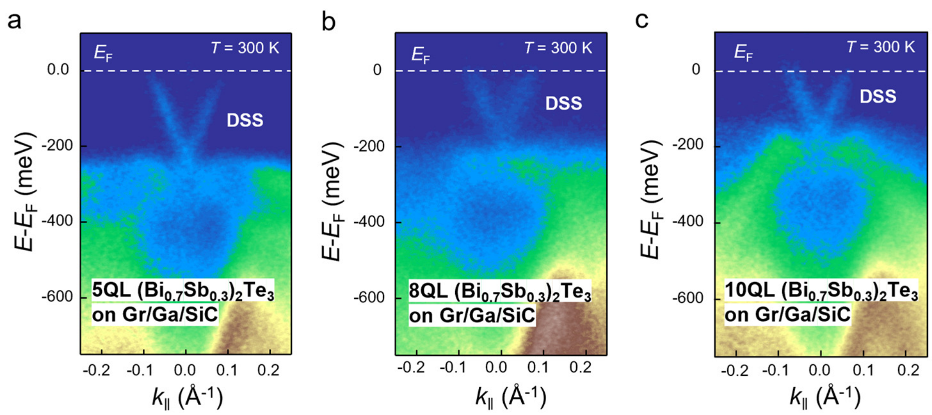

Fig. S1 | Room-temperature ARPES band maps of 5-10QL $(Bi_{0.7}Sb_{0.3})_2Te_3$ grown on Gr/Ga.

2. Fabrication of van der Waals tunnel junction

Figure S2 illustrates the steps we took to fabricate van der Waals (vdW) tunnel junctions on BST/Gr/Ga films. Grown films are transferred from the MBE chamber to an argon-filled glovebox using a vacuum suitcase with a base pressure of ~5×10^{-8} mbar and kept in the glovebox to avoid oxidization and contamination of the BST surface. We first etch a long graphite stripe (3-6 nm in thickness) into squares of approximately 3 μm^2 in area using an atomic force microscope-based etching process[1] that avoids the use of polymer resists. These graphite squares serve as the top electrodes of the tunnel junction. We then construct an h-BN/graphite electrode/1-2L h-BN stack using vdW dry transfer techniques, a picture of which is shown in Fig. S2a. The stack is transferred to a BST/Gr/Ga film inside the glovebox. Next, we use standard lithographic techniques to deposit a 55-nm-thick Al_2O_3 film to surround the h-BN encapsulated area as shown in Fig. S2b. The Al_2O_3 film further protects the BST film from oxidization and also serves to isolate individual electrodes. We subsequently use e-beam lithography and established reactive ion etch recipe (CHF_3 40 sccm/O_2 4 sccm) to open circular windows with radius about 250 nm on the top h-BN sheet to expose the graphite electrodes (Fig. S2c). Finally, we pattern and deposit 5-nm Ti/60-nm Au metal leads to connect to the graphite electrodes. The optical image of a complete device is shown in Fig. S2d. Figure S2e shows the scanning electron microscope (SEM) image of another device.

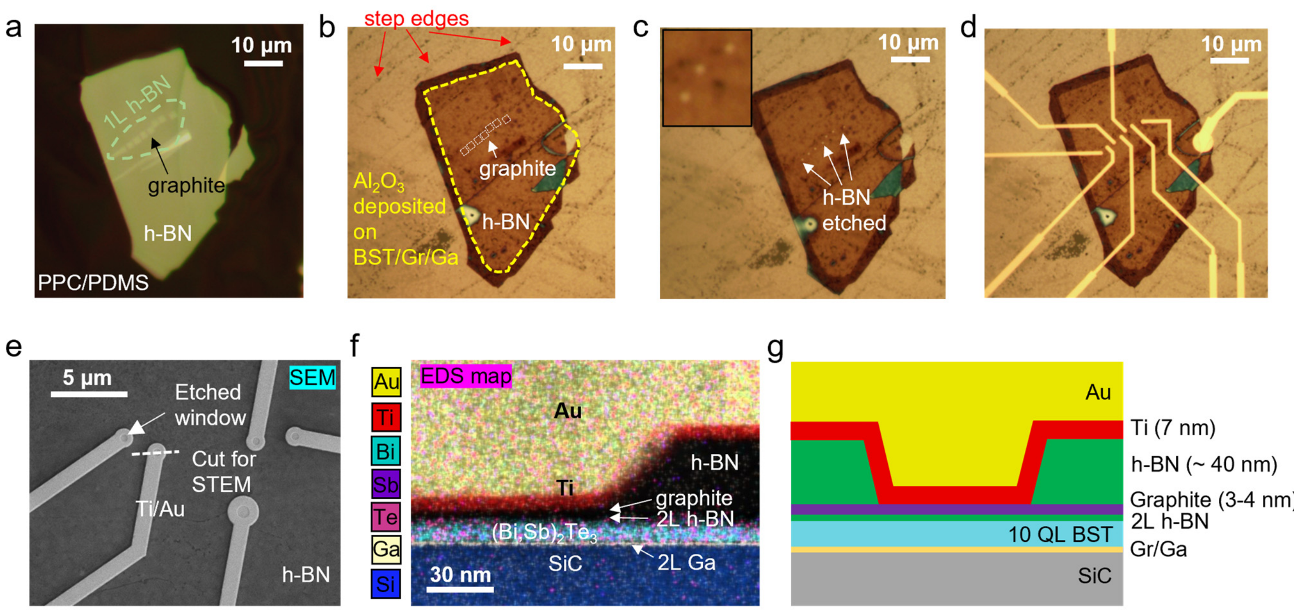

Fig. S2 | Fabrication of van der Waals tunnel junction on BST/Gr/Ga. a, A vdW stack of h-BN/graphite electrode/1L h-BN on a PPC/PDMS stamp. **b,** The stack transferred to the BST/Gr/Ga film and after the Al_2O_3 deposition. Outside the yellow dashed line, the BST/Gr/Ga film is covered with a 55nm-thick Al_2O_3 film. Red arrows point to step edges of the SiC substrate, where the intercalation of Ga may not be continuous. Tunnel junctions are placed within a single terrace. **c,** Circular windows of radius ~ 250 nm are etched into the top h-BN sheet to expose the graphite electrodes underneath. The inset shows a magnified image of a few windows. **d**, A completed device. **e,** SEM image of another device made on a 10 QL BST/Gr/Ga film. **f**, Cross-sectional EDS map of the tunnel junction. Light elements such as carbon, boron and nitrogen are not visible in this map. **g** shows a schematic diagram of the tunnel junction.

Focused ion beam (FIB) is used to cut and lift a slab along the dashed line in Fig. S2e. Scanning transmission electron microscopy (STEM) and elemental analysis are used to examine the cross sections. Figure S2f shows an energy dispersive x-ray spectroscopy (EDS) map of the van der Waals tunnel junction, with the corresponding layers labeled. This map agrees very well with the design of the structure schematically illustrated in Fig. S2g. The evaporated Au/Ti film makes contact to the graphite electrodes only.

3. Four-terminal transport on BST/Gr/Ga

We perform four-terminal transport on BST/Gr/Ga films using Hall bar devices shown in Fig. S3a. Au/Ti electrodes are evaporated to the surface of the film directly. Cross-sectional STEM images of the electrodes (Fig. S3b) show that at some locations, the metal film dips down to reach the Gr/Ga layer through voids of the BST film produced during its growth. Thus, these measurements, though conducted on the heterostructure film, reflects the superconducting properties of the 2D Ga. Fig. S3d-f show the temperature and magnetic field-dependent resistance in films of varying BST film thickness and Table S1 summarizes their growth parameters and superconducting characteristics. Overall we find the superconducting transition temperature T_c of Ga varies between 3 to 4.2 K and the out-of-plane upper critical field H_{c2} ranges 50–80 mT, consistent with previous findings of Briggs et al[2]. These measurements show that the growth of BST preserves the superconducting Ga layer very well and serve as reference to tunneling spectroscopy performed on the same films. Figure S3g plots the V- I data of a 5QL BST/Gr/Ga film, where a critical current of 200 μA is observed. Although the current flow is limited to between the current leads, we can estimate the order of magnitude of the critical current density J_c using the width of the quasi-hall bar $W = 4.7$ μm and a thickness of $d = 0.35$ nm for the 2L Ga film. J_c=0.14 A/μm^2 in this device, which is comparable to that of an elemental superconductor such as Al and Nb[3]. Measurements on other films show a typical J_c of 0.01–0.1 A/μm^2.

Film number	BST film thickness (QL)	x in $(Bi_xSb_{1-x})_2Te_3$	T_c (K)	Out-of-plane H_{c2} (mT)
01	Gr/Ga	-	3.1	79
02	5	0.7	4	80
03	10	0.7	4.1	70
04	5	0.4	3.9	47
05	8	0.7	4.2	62
06	10	0.7	3.5	73

Table S1 | Thickness, stoichiometry and superconductivity parameters of BST/Gr/Ga films studied in this work. We defined the critical temperature T_c and the upper critical field H_{c2} as the temperature and magnetic field at which the sample reaches 90% of its normal state resistance respectively.

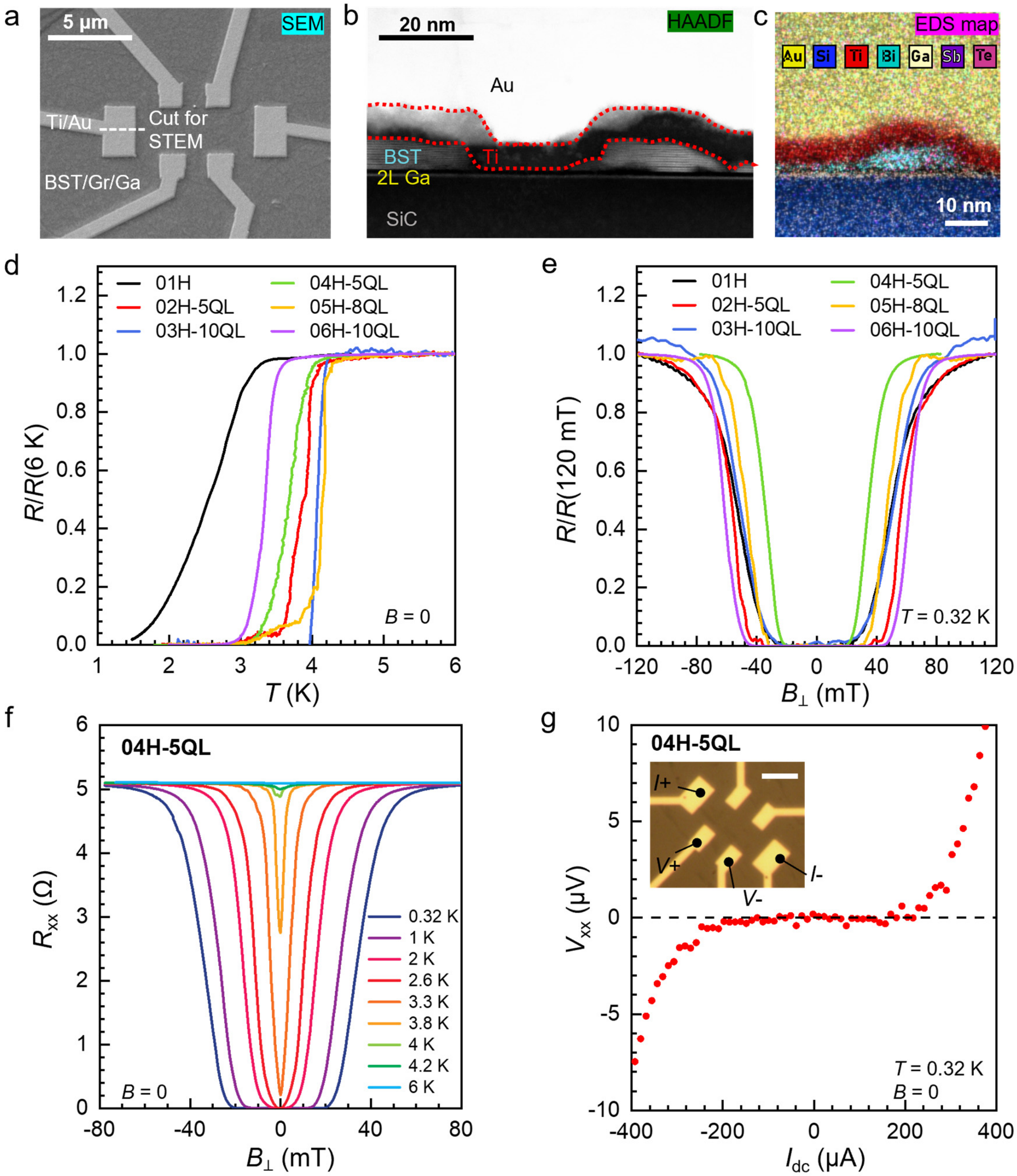

Fig. S3 | Transport studies of BST/Gr/Ga heterostructures. a, SEM image of 06H-10QL. **b**, Cross-sectional STEM image of a local area along the line cut shown in **a**. **c,** EDS map of a region close to **b** confirms the Ti layer outlined in red. It shorts to the Ga layer directly. **d**, Normalized temperature-dependent resistance $R(T)$ in devices as labeled. 01-06 correspond to the film number in Table S1. **e**, Normalized magnetic field-dependent resistance $R(B)$ of the same devices in **d**. **f**, $R(B)$ on device 04H-5QL at selected temperatures. **g**, V_{xx} versus I_{dc} on device 04H-5QL showing a large critical current of ~ 200 μA. The inset shows an optical image of the device. Metal electrodes are directly evaporated on the BST/Gr/Ga film to form a quasi-Hall bar structure. Scale bar: 5 μm.

4. Fitting the tunneling spectra on Gr/Ga using the Blonder-Tinkham-Klapwijk model

We fit the differential conductance $\mathrm{d}I/\mathrm{d}V$ vs T to the Blonder-Tinkham-Klapwijk (BTK) model (Eqs. 1-3)[4], which contains three important parameters, i.e. the superconducting gap Δ, the lifetime broadening Γ of the Cooper pairs and the tunnel barrier strength Z. A completely transparent barrier has $Z = 0$.

$$\frac{\mathrm{d}I}{\mathrm{d}V} = G_{\mathrm{N}} \int_{-\infty}^{\infty} \mathrm{d}E[1 + A(E) - B(E)] \frac{\partial f(E - \mathrm{e}V)}{\partial(\mathrm{e}V)} \Lambda(E), \tag{1}$$

where

$$A(E) = \begin{cases} \dfrac{\Delta^2}{(E + \mathrm{i}\Gamma)^2 + (1 + 2Z^2)^2[\Delta^2 - (E + \mathrm{i}\Gamma)^2]}, & E < \Delta \\ \dfrac{{u_0}^2 {v_0}^2}{\Upsilon^2}, & E \geq \Delta \end{cases} \tag{2}$$

and

$$B(E) = \begin{cases} 1 - A(E), & E < \Delta \\ \dfrac{({u_0}^2 - {v_0}^2)^2 Z^2 (1 + Z^2)}{\Upsilon^2}, & E \geq \Delta \end{cases} \tag{3}$$

with ${u_0}^2 = \frac{1}{2}\mathrm{Re}(1 + \sqrt{\frac{(E+\mathrm{i}\Gamma)^2 - \Delta^2}{(E+\mathrm{i}\Gamma)^2}})$, ${v_0}^2 = \mathrm{Re}(1 - {u_0}^2)$, and $\Upsilon^2 = [{u_0}^2 + Z^2({u_0}^2 - {v_0}^2)]^2$. $f(E) = (1 + \mathrm{e}^{E/k_{\mathrm{B}}T})^{-1}$ is the Fermi-Dirac distribution function, and $\Lambda(E)$ is the empirical instrumental broadening term with the form of $\Lambda(E) = \sqrt{2\pi\sigma^2}\exp\left(-\frac{E^2}{2\sigma^2}\right)$ where the variance σ is chosen to be 2.5 times the ac excitation $\sigma = 2.5V_{\mathrm{ac}}$ following conventional practices. We have also produced fits with $\sigma = V_{\mathrm{ac}}$ and $\sigma = 3V_{\mathrm{ac}}$ and the changes to the fitting results are negligible. Eqs. 1-3 are implemented in MATLAB to fit data.

Figure S4 shows the full set of temperature- and magnetic field-dependent tunneling spectra acquired on device 01T (Fig. S4a-c), which is a Gr/Ga film without the BST growth, together with fits using the BTK model (Fig. S4d). The resulting T-dependent SC gap $\Delta(T)$, the tunnel barrier transparency Z and the lifetime broadening Γ of the Cooper pairs are given in Fig. S4e-f. Δ(T) is well described by the BCS theory, with a $T_{\mathrm{c}} = 3.1$ K and $\Delta_0 = 0.395$ meV, consistent with four-terminal studies performed on the same film (See device 01H in Fig. S3). The tunnel barrier strength Z slightly decreases with increasing temperature while the lifetime broadening Γ increases somewhat with increasing T. These are consistent with naïve expectations. For instance, interaction with phonon modes at elevated temperatures may increase Γ while thermally assisted tunneling results in an apparent increase in the transparency of the tunnel barrier. Fitting parameters obtained here serve as reference and consistency check to analyses of the BST/Gr/Ga junctions.

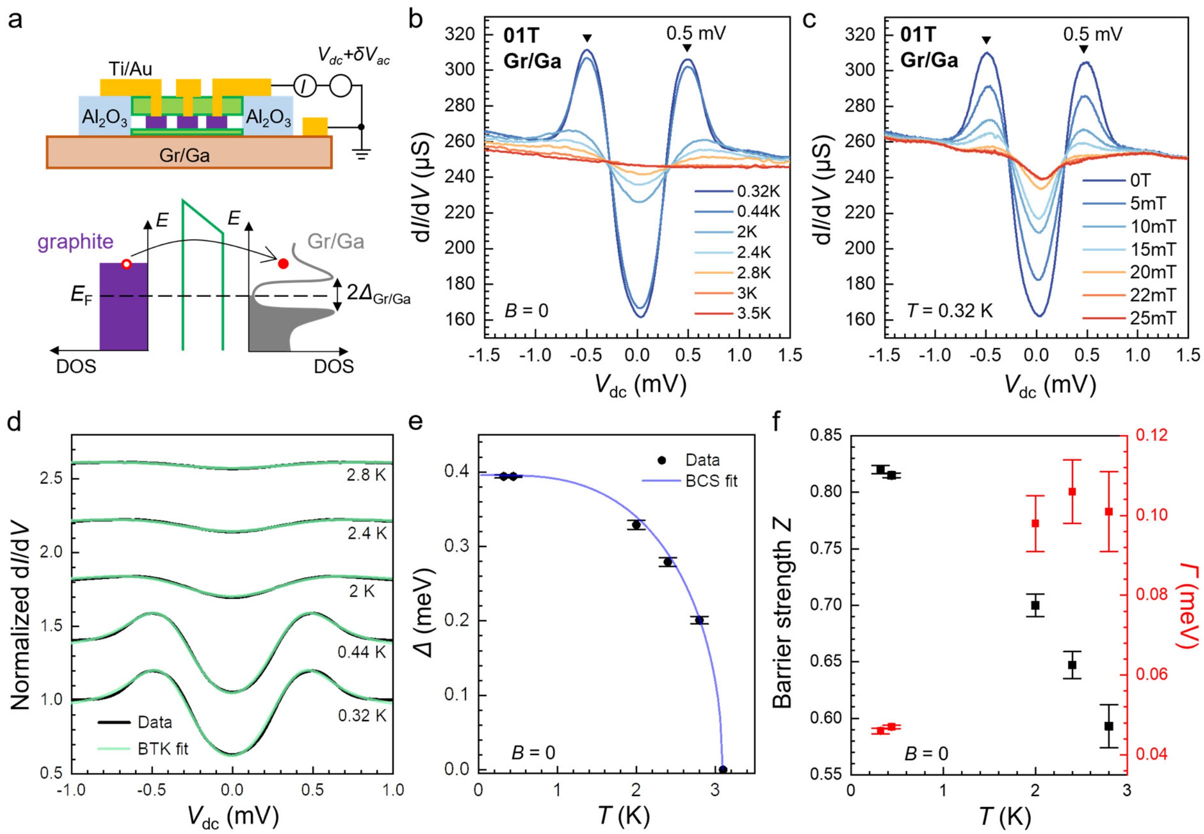

Fig. S4 | Fitting the superconducting tunneling spectra on Gr/Ga using the BTK model. a, Schematics of the tunnel junction and the tunneling process. **b**, **c,** $\mathrm{d}I/\mathrm{d}V$ versus V_{dc} on device 01T at selected temperatures (**b**), and perpendicular magnetic fields (**c**). **d**, BTK fits at different temperatures. The fits capture data very well. **e**, $\Delta(T)$ obtained from fits in **d**. The blue solid line plots the BCS description of $\Delta(T) = \Delta_0 \tanh\left(1.74\sqrt{\frac{T_c}{T} - 1}\right)$, where $T_c = 3.1$ K and $\Delta_0 = 0.395$ meV. **f**, The tunnel barrier strength parameter Z and lifetime broadening parameter Γ as a function of temperature obtained from the fits in **d**. Error bars represent 95% confidence interval of the fits.

5. Two-gap BTK fits on the 5QL and 10QL BST/Gr/Ga heterostructures

A two-gap BTK model[5] is used to fit the tunneling spectra in 5 and 10 QL TI/Gr/Ga heterostructures, where characteristics of two superconducting gaps are observed (Figs. S5 and S6). We consider the total tunneling current to be the sum of two contributions that originate from tunneling into the BST surface $(\mathrm{d}I/\mathrm{d}V)_{\mathrm{S}}$ and the BST/Gr/Ga interface $(\mathrm{d}I/\mathrm{d}V)_{\mathrm{I}}$ respectively:

$$(\mathrm{d}I/\mathrm{d}V)_{\mathrm{total}} = f_{\mathrm{S}} \times (\mathrm{d}I/\mathrm{d}V)_{\mathrm{S}} + f_{\mathrm{I}} \times (\mathrm{d}I/\mathrm{d}V)_{\mathrm{I}}, \quad (4)$$

where $f_{\mathrm{S,I}}$ represents the spectra weight of each contribution and $f_{\mathrm{S}} + f_{\mathrm{I}} = 1$. The two-gap fit contains 5 parameters, i.e, f_{S}, Δ_{S}, Δ_{I}, Γ_{S}, Γ_{I} and a common Z as it is mostly determined by the h-BN tunnel barrier.

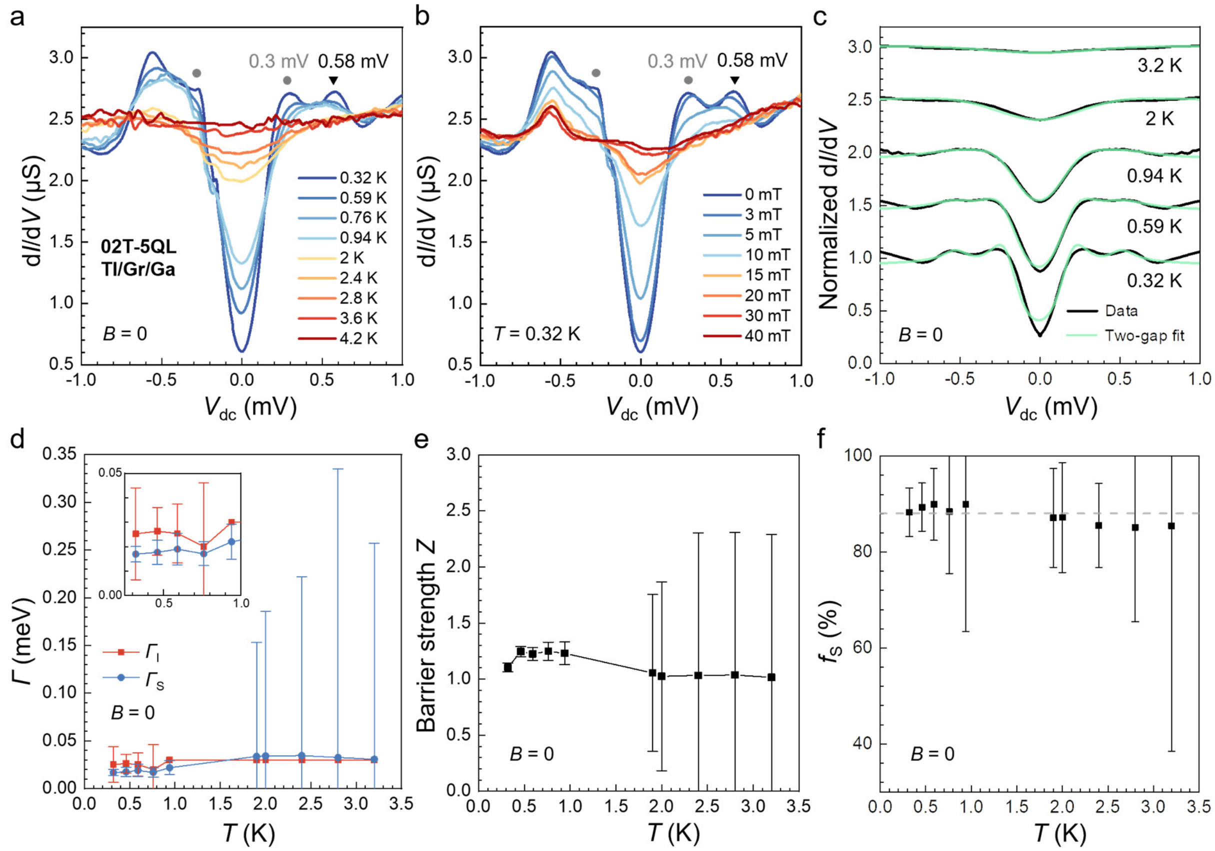

Fig. S5 | Tunneling spectra on device 02T-5QL and two-gap BTK fits. a, b, $\mathrm{d}I/\mathrm{d}V$ versus V_{dc} at selected temperatures (**a**) and perpendicular magnetic fields (**b**). **c**, Two-gap BTK fits to the data in **a** at selected temperatures. As the B-dependent spectra in **b** show, certain features on the negative bias side may not be related to superconductivity. We have therefore chosen to only fit data on the positive bias side in **c**. **d**, Lifetime broadening parameters Γ_{S} and Γ_{I} as a function of temperature obtained from the fits in **c**. The low temperature value of Γ_{I} ~0.03 meV agrees with the results in Fig. S4 very well. To reduce fitting uncertainty, we have fixed Γ_{I} ~0.03 meV for $T\sim$ 1 K and above, where $k_{\mathrm{B}}T \gg \Gamma$ and thermal broadening dominates. This allows us to obtain fits for Γ_{S}, which comes out to be similar to Γ_{I} although with large uncertainties. Part of this uncertainty originates from the anti-correlation between Γ_{S} and the barrier strength Z. A large Z reduces the zero-bias conductance, which requires a smaller Γ_{S} to compensate. **e**, The barrier strength Z as a function of temperature obtained from the fits in **c**. **f**, f_{S} as a function of temperature obtained from the fits in **c**, showing that on average, tunneling into the TI surface contributes 88% of the spectra weight. Error bars represent 95% confidence interval of the fits.

Fig. S5 show the T-dependent and B-dependent tunneling spectra taken on device 02T-5QL, the BTK fits, and the parameters obtained from the fits. The main results, i.e. $\Delta_{\mathrm{S}}(T)$ and $\Delta_{\mathrm{I}}(T)$, are shown in Fig. 3 of the main text. Figs. S5d-f plot the remaining fitting parameters. The two-gap fits yield robust values of Δ_S and Δ_I, especially at low temperatures, as their values are dictated by prominent features of the data such as the V shape near zero bias and the appearance of a second coherence peak. A barrier strength of Z ~1 is consistent among all the junctions we analyzed (Figs S4-6). The results for the lifetime broadening parameters are less reliable at $T > 1$ K where features become broadened and independent determinations become difficult. Nonetheless, they are consistent with results obtained on Gr/Ga junctions (Fig. S4) and on a 10QL BST/Gr/Ga heterostructure (Fig. S6). Our fits show that the measured $\mathrm{d}I/\mathrm{d}V$ is dominated by the tunneling into the TI surface states, with f_S ~0.9. This is also reasonable, given that an electron reaching the Gr/Ga interface needs to traverse the semi-insulating $(Bi_{0.7}Sb_{0.3})_2Te_3$ bulk.

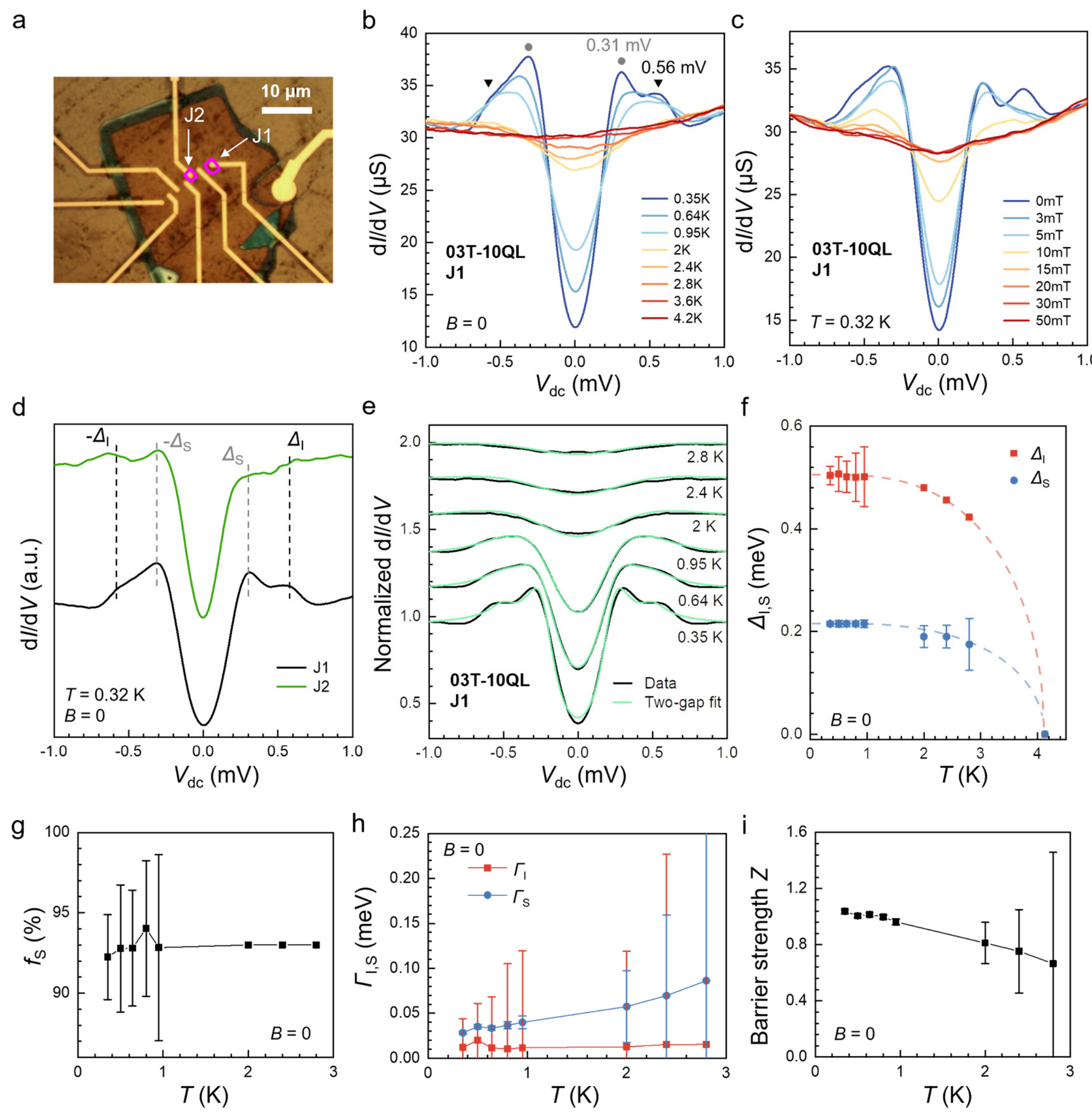

Fig. S6 | Tunneling spectra on device 03T-10QL and two-gap BTK fits. a, Optical image of 03T-10QL made on a 10QL $(Bi_{0.7}Sb_{0.3})$/Gr/Ga film. J1 and J2 are two independent junctions. **b, c,** $\mathrm{d}I/\mathrm{d}V$ versus V_{dc} at selected temperatures (**b**) and perpendicular magnetic fields (**c**) from J1. **d** plots the $T = 0.32$ K $\mathrm{d}I/\mathrm{d}V$ traces from both junctions J1 and J2. Curves are normalized by their normal state conductance and stacked vertically for clarity. **e**, Two-gap BTK fits to the data in **a** at selected temperatures. Only data at positive biases are analyzed. Data at negative biases are replica of the positive side. **f**, $\Delta_{\mathrm{S}}(T)$ and $\Delta_{\mathrm{I}}(T)$ obtained from the fits in **e**. The red and blue dashed lines represent fits to the temperature dependence of a BCS gap with a common $T_{\mathrm{c}} =$ 4.1 K, similar to Fig. 3e of the main text. **g**, f_{S} as a function of temperature obtained from the fits in **e** showing that below 1 K, 93% of the tunneling current goes into the TI surface. Above 2 K, f_{S} is fixed at 0.93 to enable more accurate fits for other parameters. **h**, Lifetime broadening parameters Γ_{S} and Γ_{I} as a function of temperature obtained from the fits in **e**. Values obtained here are consistent with those found in Figs. S4 and S5. **i,** Barrier strength Z as a function of temperature obtained from the fits in **e**, which is also consistent with other junctions studied. Error bars represent 95% confidence interval of the fits.

Similar tunneling spectroscopy measurements and analysis are performed on two other T-5QL junctions made on film 02 and two T-10QL junctions made on film 03. Features associated with two SC gaps are consistently observed in all of our devices, confirming that a proximity-induced gap opening in the surface states of the BST film is a robust finding of our experiment. The measurements and analysis of 03T-10QL are shown in Fig. S6.

Table S2 summarizes the proximity-induced Δ_S and the primary superconducting gap Δ_I obtained in different tunnel junctions made on BST films of different thicknesses d. The thickness dependence of Δ_S is not evident, likely due to the local variations of the film thickness under each junction. A study of $\Delta_S(d)$ will require a more precise control of the film thickness.

BST film thickness (QL)	T_c (K)	Junction	Δ_I (meV)	Δ_S (meV)	Δ_S/Δ_I (%)
0	3.1	01T	0.395 ± 0.003	-	-
5	4	G_{15} of 02T-5QL	0.5 ± 0.03	0.19 ± 0.01	37 ± 4
		G_{25} of 02T-5QL	0.49 ± 0.05	0.2 ± 0.003	41 ± 4
		G_{45} of 02T-5QL	0.51 ± 0.03	0.23 ± 0.01	46 ± 5
10	4.1	J1 of 03T-10QL	0.5 ± 0.02	0.215 ± 0.004	42 ± 2
		J2 of 03T-10QL	0.5 ± 0.03	0.17 ± 0.01	34 ± 4

Table S2 | Δ_I, Δ_S, and the ratio Δ_S/Δ_I found in different devices. Δ_I= Δ_0 in Gr/Ga.

6. Evidence of Abrikosov vortex probed by tunneling conductance

Discrete zero-bias conductance changes and hysteresis in *B*-field sweep due to the bunching and trapping of Abrikosov vortices are commonly observed in Gr/Ga and BST/Gr/Ga films we studied. Fig. S7a, c provide additional examples in devices 01T Gr/Ga and 02T-5QL BST/Gr/Ga. We identify the unit of conductance change G_{sv}, which all other conductance jumps are multiple integers of, and attribute it to the entry/exit of a single vortex. This enables us to calculate the number of vortices N_{vortex} in the tunnel junction using

$$N_{vortex} = \frac{G(B) - G(0T)}{G_{sv}}, \tag{5}$$

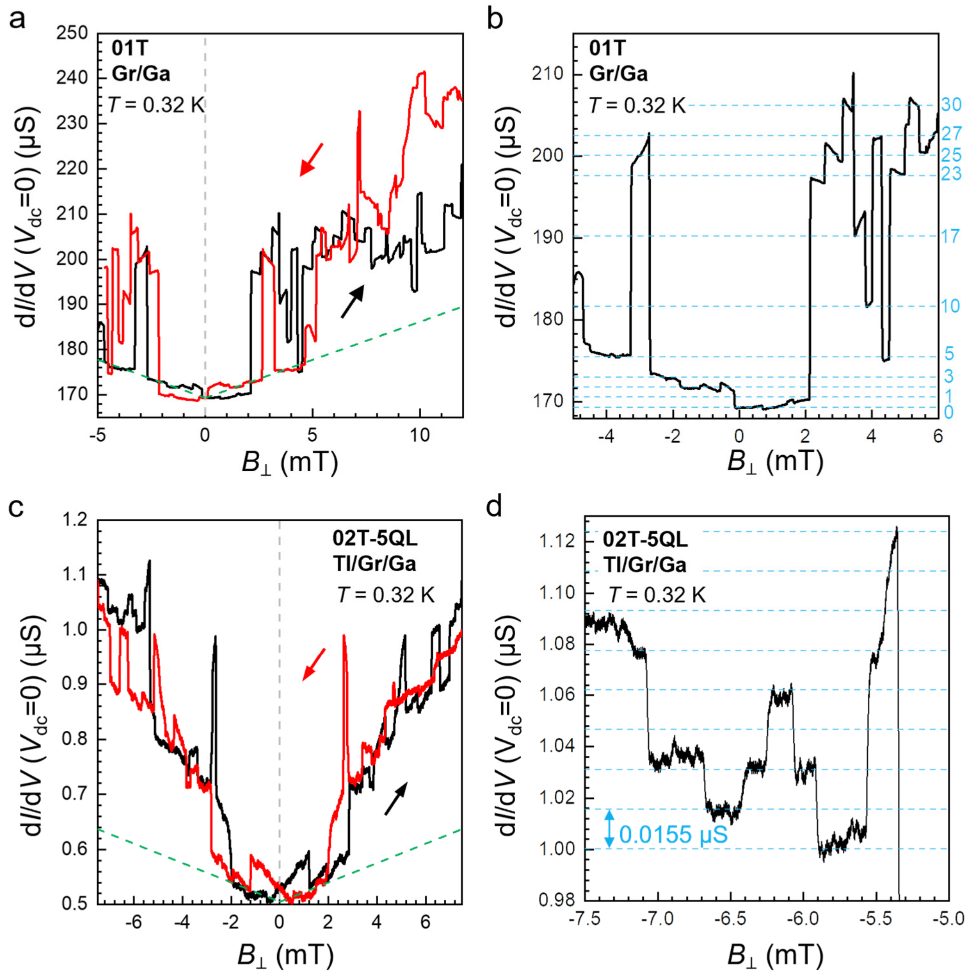

Fig. S7 | Single vortex signature and vortex pinning in Gr/Ga and TI/Gr/Ga films. a, Zero-bias $\mathrm{d}I/\mathrm{d}V$ versus $B_\perp$ in device 01 T (**a**) and 02T-5QL (**c**) showing hysteresis and discrete conductance jumps. The green dashed line is the calculated $\Delta G/\Delta B$ using Eq. (6) and the junction area $A = 2.82\ \mu\mathrm{m}^2$ in **a** and $A = 2.49\ \mu\mathrm{m}^2$ in **c**. The magnetic field is swept at a slow rate of 5–10 $\mu\mathrm{T/s}$ to allow for the establishment of steady state. $T = 0.32$ K. **b**, Conductance plateaus in **a** are labeled by N_{vortex} given by Eq. (5). $G_{\mathrm{sv}} = 1.23\ \mu\mathrm{S}$. **d**, Expanded data around $B_\perp = -6.5$ mT in **c** showing discrete conductance jumps in units of 1, 2, and 3 G_{sv}, where $G_{\mathrm{sv}} = 0.0155\ \mu\mathrm{S}$ corresponds to the minimum conductance jump due to a single vortex.

We label N_{vortex} corresponding to individual conductance plateaus in device 01T in Fig. S7b. Figure S7d shows examples of 1, 2, and 3 vortex-induced conductance change in 02T-5QL. As B increases, the number of vortices increases following $\Phi = B \times A = N_{\mathrm{vortex}} \times \Phi_0$, where A is the tunnel junction area given by the top graphite electrode and $\Phi_0 = 2.068\ \mathrm{mT} \cdot \mu\mathrm{m}^2$ is the magnetic flux quantum. Together with Eq. (5), we obtain the average rate of conductance change vs B-field:

$$\frac{\Delta G}{\Delta B} = \frac{A \times G_{\mathrm{sv}}}{\Phi_0}. \qquad (6)$$

Eq. (6) is plotted as a green dashed line in Figs. S7a and c for devices 01T and 02T-5QL respectively. They capture the trend of data around $B = 0$ quite well. At B greater than a few mT, the conductance fluctuates both up and down with large amplitude, suggesting vortices move in and out of the tunnel junction area as bundles[6]. We expect that defects, such as domain walls in the film, to play an important role in the bunching and pinning of the vortices and details will vary from film to film and junction to junction. Indeed, Fig. S8 compares J1 and J2 made on the same film 03. J1 exhibits much larger conductance fluctuations than J2, suggesting stronger pinning effects.

a

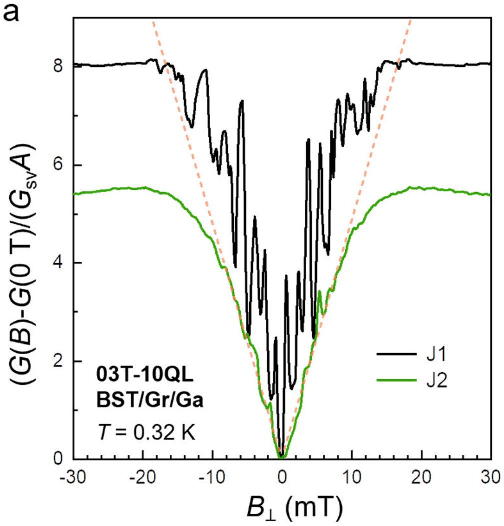

b

	Area A (μm^2)	Conductance of a single vortex G_{sv} (μS)
J1	3.84	0.5
J2	3.38	1.7

Fig. S8 | Vortex pinning in different junctions made on 03T-10QL. a, plots the vortex density N_{vortex}/A calculated from $\frac{G(B)-G(0\ \mathrm{T})}{G_{\mathrm{sv}}\times A}$ for junctions J1 and J2, respectively. The orange dashed line plots B/Φ_0. By definition, $N_{\mathrm{vortex}}/A = B/\Phi_0$. J2 follows the orange dashed line very well, indicating smooth evolution of the Abrikosov vortex lattice while J1 exhibits large deviations from the expected rate, suggesting strong pinning effects. Field sweep rate: 100 µT/s. Parameters used in the analysis are given in **b**. Data of J2 are shown in Fig. 4 of the main text.

References

1. Li, H.Y., Ying, Z., Lyu, B.S., Deng, A.L., Wang, L.L., Taniguchi, T., Watanabe, K., Shi, Z.W., Electrode-Free Anodic Oxidation Nanolithography of Low-Dimensional Materials. *Nano Lett.* **18**, 8011-8015 (2018).

2. Briggs, N., Bersch, B., Wang, Y.X., Jiang, J., Koch, R.J., Nayir, N., Wang, K., Kolmer, M., Ko, W., Duran, A.D., Subramanian, S., Dong, C.Y., Shallenberger, J., Fu, M.M., Zou, Q., Chuang, Y.W., Gai, Z., Li, A.P., Bostwick, A., Jozwiak, C., Chang, C.Z., Rotenberg,

E., Zhu, J., van Duin, A.C.T., Crespi, V., Robinson, J.A., Atomically thin half-van der Waals metals enabled by confinement heteroepitaxy. *Nat. Mater.* **19**, 637–643 (2020).

3. Talantsev, E.F., Crump, W.P., Tallon, J.L., Universal scaling of the self-field critical current in superconductors: from sub-nanometre to millimetre size. *Sci. Rep.* **7**, 10010 (2017).

4. Blonder, G.E., Tinkham, M., Klapwijk, T.M., Transition from metallic to tunneling regimes in superconducting microconstrictions: Excess current, charge imbalance, and supercurrent conversion. *Phys. Rev. B* **25**, 4515-4532 (1982).

5. Daghero, D., Gonnelli, R.S., Probing multiband superconductivity by point-contact spectroscopy. *Supercond. Sci. Technol.* **23**, 043001 (2010).

6. Suderow, H., Guillamon, I., Rodrigo, J.G., Vieira, S., Imaging superconducting vortex cores and lattices with a scanning tunneling microscope. *Supercond. Sci. Technol.* **27**, 063001 (2014).